JACS
JOURNAL OF THE AMERICAN CHEMICAL SOCIETY
pubs.acs.org/JACS
Article

# Frequency-Agile Low-Temperature Solution-Processed Alumina Dielectrics for Inorganic and Organic Electronics Enhanced by Fluoride Doping

Xinming Zhuang, Sawankumar Patel, Chi Zhang, Binghao Wang, Yao Chen, Haoyu Liu, Vinayak P. Dravid,* Junsheng Yu,* Yan-Yan Hu,* Wei Huang,* Antonio Facchetti,* and Tobin J. Marks*

Cite This: J. Am. Chem. Soc. 2020, 142, 12440−12452



**ABSTRACT:** The frequency-dependent capacitance of low-temperature solution-processed metal oxide (MO) dielectrics typically yields unreliable and unstable thin-film transistor (TFT) performance metrics, which hinders the development of next-generation roll-to-roll MO electronics and obscures intercomparisons between processing methodologies. Here, capacitance values stable over a wide frequency range are achieved in low-temperature combustion-synthesized aluminum oxide ($AlO_x$) dielectric films by fluoride doping. For an optimal F incorporation of ∼3.7 atomic % F, the F:$AlO_x$ film capacitance of 166 ± 11 nF/cm$^2$ is stable over a $10^{-1}$−$10^4$ Hz frequency range, far more stable than that of neat $AlO_x$ films (capacitance = 336 ± 201 nF/cm$^2$) which falls from 781 ± 85 nF/cm$^2$ to 104 ± 4 nF/cm$^2$ over this frequency range. Importantly, both n-type/inorganic and p-type/organic TFTs exhibit reliable electrical characteristics with minimum hysteresis when employing the F:$AlO_x$ dielectric with ∼3.7 atomic % F. Systematic characterization of film microstructural/compositional and electronic/dielectric properties by X-ray photoelectron spectroscopy, time-of-fight secondary ion mass spectrometry, cross-section transmission electron microscopy, solid-state nuclear magnetic resonance, and UV−vis absorption spectroscopy reveal that fluoride doping generates AlOF, which strongly reduces the mobile hydrogen content, suppressing polarization mechanisms at low frequencies. Thus, this work provides a broadly applicable anion doping strategy for the realization of high-performance solution-processed metal oxide dielectrics for both organic and inorganic electronics applications.

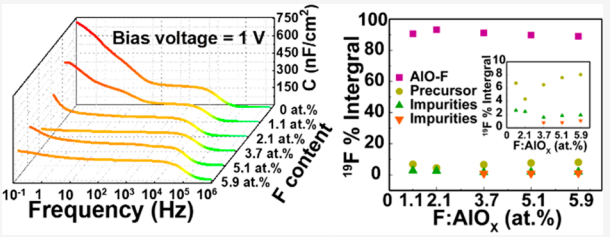


## INTRODUCTION

Solution-processed (semi)conducting and insulating metal oxide (MO) films have attracted great research interest because of their low-temperature large-area processability in ambient, good carrier mobility, high dielectric constants, excellent optical transparency in the visible region, mechanical flexibility, and electrical/morphological uniformity over large areas. These properties make them attractive candidates for optically transparent and roll-to-roll compatible next-generation electronics.[1−8] Furthermore, compared with conventional semiconductors that can be effectively processed solely by vapor-phase deposition methods such as atomic layer deposition, chemical vapor deposition, and sputtering, MOs can be solution-processed in ambient which should significantly lower production costs and increase fabrication throughput.[9−15] Indeed, several studies have shown excellent (semi)conductor/dielectric metal oxide performance for solution processed films. Among them, combustion synthesis, "sol-gel on chip", and deep UV illumination have achieved the best MO films for fabrication temperatures below 300 °C or even near room temperature.[16−21]

Solution processed metal oxide dielectrics [e.g., yttrium oxide, hafnium oxide, zirconium oxide, and aluminum oxide ($AlO_x$)] processed at low temperature have also been studied with the objective of displacing their counterparts grown by energy-intensive vapor phase techniques.[1,2] High performance oxide transistors based on these low-temperature solution processed dielectrics were reported to exhibit very low driving voltages and extraordinarily high electron mobilities.[22,23] For example, Xu et al. demonstrated aqueous route based $In_2O_3$/$Al_2O_3$ TFTs with a high mobility of 30.9 cm$^2$/(V s) and a low operating voltage of 4 V for a maximum processing temperature of 250 °C.[24] Using a combination of solution combustion synthesis and ultraviolet treatment of $HfO_x$, Fortunato et al. reported gallium−indium−zinc oxide

Received: May 11, 2020
Published: June 15, 2020

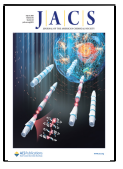

(IGZO) TFTs with a high saturation mobility (43.9 $cm^2/(V\ s)$) and a low operating voltage (<3 V) for low processing temperatures (150 °C).[25] Combining a $SnO_2$ film channel and a sol−gel processed $ZrO_2$ high-dielectric constant ($\kappa$) dielectric layer, Subramanian et al. reported exceptionally high performance TFTs with a mobility of ∼100 $cm^2/(V\ s)$ operating at a voltage <1.5 V for a maximum process temperature of 400 °C.[26] Shan et al. produced $In_2O_3$ TFTs with a high mobility of 23.6 $cm^2/(V\ s)$ and a low operating voltage of 1.5 V by combining UV/ozone treatment with a low-temperature (300 °C) annealed $ZrO_x$ gate dielectric.[27]

It is worth noting that, for a given oxide semiconductor, transistors using solution-processed oxide gate dielectrics consistently outperform those based on high-quality gate dielectrics fabricated by conventional thermal ($SiO_2$) or ALD-($AlO_x$) methodologies.[28−30] Nevertheless, few studies have addressed the mechanism of the enhanced TFT mobility for solution-processed MO dielectrics. For example, Zeumault et al. proposed that mobility enhancement in oxide TFTs was attributable to the presence of donor-like electron traps in solution-processed $ZrO_2$ dielectrics.[31] Alshareef and co-workers proposed that the presence of hydroxyl groups on the $AlO_x$ dielectric film surface facilitates unintentional Al-doping, leading to enhanced device performance.[32] In addition, a systematic mobility analysis versus the areal gate capacitance of solution-processed oxide TFTs by Lee et al. found that by increasing the areal gate capacitance (increased charge density) by using a high $\kappa$ dielectric led to higher field-effect mobilities due to effective trap passivation.[33]

In contrast to the above results, Sirringhaus et al. reported that hydrogen ion migration in low-quality $Al_2O_3$ dielectrics produces long-lived dipolar disorder and dielectric instability.[34] Chemical analysis based on dynamic-secondary ion mass spectrometry (SIMS), 3D-time-of-fight secondary ion mass spectrometry (3D-TOF-SIMS), X-ray photoelectron spectroscopy (XPS), and reflection electron energy loss spectroscopy (REELS) argued that the induced dipole effect is related to significant residual hydrogen concentrations in low-temperature processed MO dielectrics. Thus, extracted mobilities are far larger than those in high-quality samples and there is significant $I-V$ hysteresis in the TFT transfer curves.[35,36] Among the proposed mechanisms, this laboratory found that the presence of mobile hydrogen ions in the gate dielectric agrees with findings on low-temperature solution-processed dielectrics, where distinct anticlockwise hysteresis is seen in the transfer characteristics of n-type MO transistors.[31,37−39] According to previous studies, mobile hydrogen ions contribute to slow polarization of the bulk dielectric, resulting in much higher capacitance at low frequencies versus the typical frequencies ($\geq 10^3$ Hz) used to measure the gate dielectric capacitance.[40] Thus, since TFT measurements are usually carried out at quasi-static conditions (<10 Hz), using the high-frequency capacitance value to extract the mobility significantly overestimates the field-effect mobility.[25,28]

Cation doping of gate dielectrics (e.g., La in $AlO_x$) has been used to mitigate the substantial capacitance−frequency dependence at low frequencies (∼10 Hz) and yields hysteresis-free transistor performance and reliable mobilities.[34] Other than MO cation doping,[41−44] anion doping has also been explored to modulate MO properties, especially for MO semiconductors.[45−48] Moreover, this laboratory recently found that incorporating fluoride (F) in both the solution-processed semiconductor ($InO_x$) and dielectric ($AlO_x$) films promotes metal coordination and impurity removal, leading to high-performance amorphous oxide TFTs.[49] However, we did not explore the details of how anion doping enhances the dielectric stability at low frequencies or study the doping mechanism. Understanding how key dielectric parameters (capacitance-frequency relationships, leakage currents, breakdown fields, and interfacial properties) are affected by anion doping is critical for enabling high-performance transistors particularly when processed at low temperatures.

In this contribution, we demonstrate that low-temperature (250−300 °C) solution-processed $AlO_x$ films with excellent dielectric properties and frequency stability are achieved by fluoride doping. By carefully tuning the $AlO_x$ fluoride content from 0.0 at. % to ∼6 at. %, fluoride-doped (F:$AlO_x$) films exhibiting stable dielectric response over a wide frequency range (e.g., for F content = 3.7 at. %, $\kappa$ = 4.3−3.4 at 0.1−$10^4$ Hz) and excellent dielectric strength (e.g., for F content = 3.7 at. %, 7.0 MV/cm) are realized. Our results show that the enhanced dielectric properties are attributable to oxyfluoride formation in the dielectric bulk, reducing the mobile hydrogen ion content and suppressing electron trap formation in $AlO_x$. Both n-type ($In_2O_3$) and p-type (organic semiconductor) transistors with F:$AlO_x$ gate dielectrics exhibit neglectable hysteresis and reliable transport characteristics, which are similar to those reported for control devices fabricated with high-quality thermal $SiO_x$ gate dielectrics. Thus, this work establishes a new expeditious route for the realization of high-quality solution-processed dielectric films for transistor circuitry.

## EXPERIMENTAL SECTION

**Precursor Preparation.** $Al(NO_3)_3{\cdot}9H_2O$ and $In(NO_3)_3{\cdot}xH_2O$ (99.999%) were purchased from Sigma-Aldrich and used without further purification. For $AlO_x$ precursor preparation, 93.78 mg of $Al(NO_3)_3$ were dissolved in 5.0 mL of 2-ME. Next, 25 $\mu$L of acetylacetone (AcAc) and 11.25 $\mu$L of 14.5 M $NH_3$(aq) were added and the solution was stirred overnight (∼10 h) before film fabrication. For the F-doping (F:$AlO_x$), the precursor 1,1,1-trifluoro-2,4-pentanedione in 0, 5, 10, 20, 30, and 40 wt % to the total weight of $Al(NO_3)_3$ was added to the above precursor solutions 1 h before spin-coating. For $In_2O_3$ precursor preparation, $In(NO_3)_3{\cdot}xH_2O$ was dissolved in deionized water to achieve a 0.1 M In concentration and the precursor solution was stirred for 8 h before use.

**Thin-Film Fabrication and Electrical Characterization.** All the solutions were filtered through 0.2-$\mu$m PTFE syringe filters before fabrication. n++ silicon wafer substrates were ultrasonically cleaned in IPA and then with an oxygen plasma for 15 min before use. The $AlO_x$ and F:$AlO_x$ precursor solutions were then spin-coated onto the substrates at 3500 rpm for 30 s in a controlled atmosphere box [relative humidity (RH) < 20%] and preannealed at 120 °C for 60 s (RH ∼35%), followed by annealing on a 250 or 300 °C hot plate for 1 min (RH ∼35%). The fabrication process involves combustion synthesis, which generates a large amount of heat during MO precursor decomposition in a short time. Moreover, the first step of preannealing at 120 °C/60 s yields dry MO-precursor films and removes extraneous solvent from the precursor films before combustion onset, and dramatically shortens the processing/annealing time. Hence, only 1 min is required for the annealing process of F:AlOx.[49] Note that controlling the humidity level during coating and annealing is particularly important to obtain uniform and reproducible MO films. This process was repeated four times to obtain the desired film thickness (∼20 nm). For capacitors, 40 nm Au was thermally evaporated through a shadow mask to form a 200 × 200 $\mu m^2$ top electrode. Capacitor characterization was performed under ambient in the dark on a custom probe station using an Agilent 1500 semiconductor parameter analyzer or a Bio-Logic SP-150


https://dx.doi.org/10.1021/jacs.0c05161
J. Am. Chem. Soc. 2020, 142, 12440−12452

analyzer. For the $In_2O_3$ TFT fabrication, the $In_2O_3$ precursor solution was spin-coated at 3000 rpm for 20 s on $AlO_x$ and F:$AlO_x$ films and then annealed on a hot plate at 250 °C for 20 min. This process was repeated three times to achieve the desired semiconductor film thickness of ∼10 nm. Finally, 40 nm Al was thermally evaporated to form source/drain electrodes with a channel length of 100 $\mu$m and channel width of 1500 $\mu$m. For the pentacene (P5) TFT fabrication, a 30 nm P5 film was vacuum-deposited at a rate of ∼0.05 nm $s^{-1}$ (∼5 × $10^{-6}$ Torr). For the TIPS-P5 and DPP-DTT TFT fabrication, TIPS-P5 active layers were spin-coated at 1500 rpm for 50 s from 5 mg $mL^{-1}$ 1,2-dichlorobenzene solutions and were then thermally annealed on a 100 °C hot plate for 20 min. DPP-DTT active layers were spin-coated at 1500 rpm for 30 s from 5 mg $mL^{-1}$ chloroform solutions and were then thermally annealed on a 200 °C hot plate for 30 min. Then, 40 nm Au source/drain electrodes were thermally evaporated to form a channel length of 100 $\mu$m and channel width of 1500 $\mu$m. TFT characterization was performed under ambient in the dark on a custom probe station using an Agilent 1500 semiconductor parameter analyzer. Although the channels of these transistors are not patterned, the mobility measured should be accurate since the source/drain $W/L$ ratio is within a range accepted by the community.[8,15]

**Oxide Film Characterization.** Atomic force microscopy (AFM) film topographies were imaged with a Veeco Dimension Icon scanning Probe Microscope using tapping mode. Grazing-incidence X-ray diffraction (GIXRD) and X-ray reflectivity (XRR) measurements were carried out with a Rigaku SmartLab Thin-film Diffraction Workstation using a high intensity 9 kW Cu rotating anode X-ray source coupled to a multilayer optic. XPS was performed on Thermo Scientific ESCALAB 250Xi at a base pressure of 4.5 × $10^{-10}$ mbar (UHV). Spectra were obtained after the surface of the film was etched for ∼2 nm to minimize surface contamination. Elemental depth profiling was also carried out with ToF-SIMS (PHI TRIFT III). Cross-sectional STEM images and EDS maps were performed with a Cs-corrected JEOL ARM 200CF operated at 200 kV, with samples prepared on Si using focused ion beam (FIB) techniques (FEI Helios NanoLab 600). A thin Au layer was deposited on the sample surface to protect from damage during the FIB processing. Both DSC and TGA measurements were performed on an SDT Q60 instrument (TA Instruments, Inc.). NMR experiments were carried out at the NSF-supported NHMFL, and F:$AlO_x$ powders were prepared by drop-casting appropriate oxide precursor solutions on Si substrates at 120 °C for 60 s (RH ∼35%), followed by annealing on a 300 °C hot plate for 1 min (RH ∼35%). This process was repeated ∼40 times to achieve ∼10 mg samples. $^{19}$F NMR experiments were conducted at 470 MHz (11.8 T) on a Bruker Avance-III 500 spectrometer using a 2.5 mm Bruker probe. Spectra were obtained using a rotor-synchronized spin−echo pulse sequence with a 90° pulse length of 4 $\mu$s and a recycle delay of 300 s at a spin rate of 25 kHz. The chemical shift of $^{19}$F NMR spectra was calibrated with LiF at −201.2 ppm. $^{27}$Al NMR experiments were conducted on an 830 MHz spectrometer at a Larmor frequency of 216 MHz at a spinning rate of 14 kHz. The spectra were acquired using a single $\pi/8$ pulse of 0.5 $\mu$s to observe the central transition peak with a recycle delay of 1 s. The resonance was calibrated using 1 M $Al(NO_3)_3$ at 0 ppm. $^1$H NMR spectra were collected on a 600 MHz spectrometer with a 1.3 mm probe spinning at 50 kHz. The rotor-synchronized spin−echo was used to collect $^1$H spectra with a 90° pulse length of 2.9 $\mu$s. The resonance was calibrated using adamantane at 1.83 ppm. UV−vis absorption measurements were carried out with the PerkinElmer LAMBDA 1050 instrument.

## RESULTS AND DISCUSSION

**Dielectric Film Fabrication and Characterization.** $AlO_x$ was selected for fluoride doping experiments, since it is one of the most investigated solution processed gate dielectric materials[50,51] that undergoes F-doping,[52] and has been the subject of much recent effort to achieve high-quality solution-processed dielectric films below 300 °C.[53,54] The present F:$AlO_x$ films were fabricated by combustion synthesis[16,21] using $Al(NO_3)_3$ as the Al source/oxidizer (0.05 M in 2-ME), acetylacetone (AcAc), $NH_3$(aq) (14.5 M) as the fuel, and 1,1,1-trifluoroacetylacetone (FAcAc, Figure 1a) as the F source

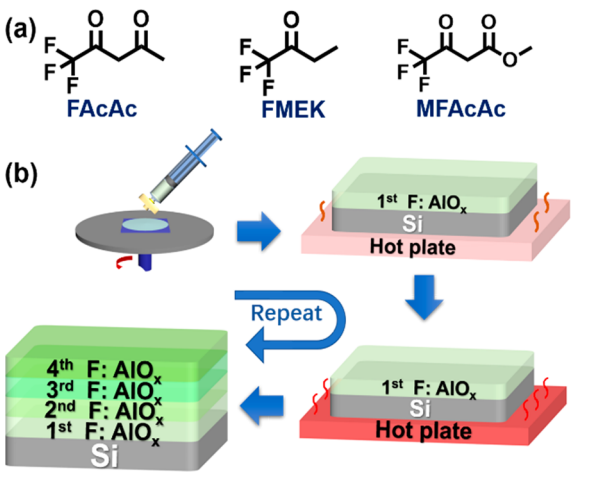


**Figure 1.** (a) Molecular structures of 1,1,1-trifluoro-2-butanone (FMEK), methyl 4,4,4-trifluoroacetoacetate (MFAcAc) and 1,1,1-trifluoro-2,4-pentanedione (FAcAc). (b) Schematic of F:$AlO_x$ dielectric film fabrication process.

after screening several candidates (1,1,1-trifluoro-2-butanone (FMEK) and methyl 4,4,4-trifluoroacetylacetone (MFAcAc); *vide infra* for details. FAcAc additions of 0, 5, 10, 20, 30, and 40 wt % vs $Al(NO_3)_3$ were used to achieve F:$AlO_x$ with F incorporation levels varying from 0 at. % to ∼6 at. % vs Al. Film fabrication consisted of first spin-coating the precursor solutions onto Si substrates ($n^{++}$) followed by thermal annealing on a hot plate at 250 or 300 °C for 1 min. The spin-coating and annealing process is repeated four times to yield the dielectric films with a thickness of ∼20 nm (Figure 1b). Details regarding the fabrication process can be found in the Experimental Section.

We find that 300 °C is the optimal processing temperature; thus, the 300 °C annealed films are first reported and primarily discussed. XPS was performed to monitor the chemical composition of the F:$AlO_x$ films (Figure S1). As shown in Figure 2a and Table S1, the F content in the $AlO_x$ matrix steadily increases from 0 to 1.1, 2.1, 3.7, 5.1, and 5.9 at. %, as the FAcAc quantity in the precursor is increased from 0 wt % to 5, 10, 20, 30, and 40 wt %, respectively. Note, in the neat $AlO_x$, ∼3 at. % carbon (C 1s) is detected, which remains below ∼6 at. % even with up to 40 wt % of FAcAc. Thus, most of the C from this precursor is removed during combustion. The O/Al atomic ratio remains at ∼1.8 for the different levels of F incorporation, indicating an O-rich environment where the O excess likely includes C−O containing species (Figure S1).

Importantly, XPS reveals that the F 1s binding energy is ∼685.5 eV in these F:$AlO_x$ films (Figure 2b), indicating that the vast majority of the F is bonded to Al[55,56] rather than present as organic fluoride.[57,58] Furthermore, the Al 2p and O 1s binding energies exhibit a shift toward higher values as the F-doping level increases, from 74.2 and 530.8 eV in neat $AlO_x$ to 75.0 and 531.5 eV in the 5.9 at. % F:$AlO_x$ sample, respectively (Figure 2c and 2d). It is known that in $AlF_3$ the Al 2p binding energy feature is at ∼77.2 eV and, upon incorporating additional oxyfluoride in $AlO_x$, a positive binding energy shift of both the Al 2p and O 1s signals is


https://dx.doi.org/10.1021/jacs.0c05161
J. Am. Chem. Soc. 2020, 142, 12440−12452

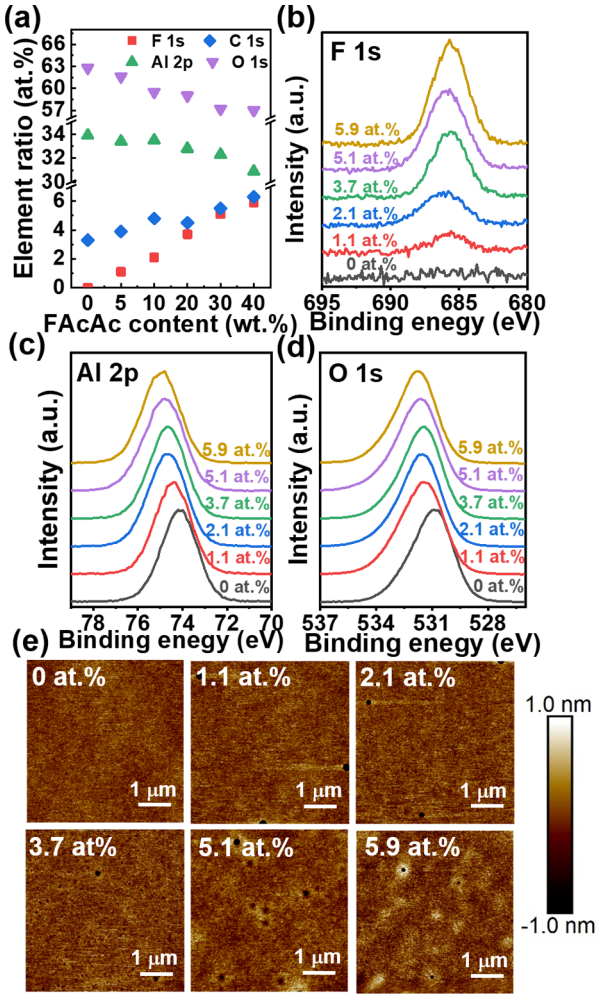


**Figure 2.** (a) Elemental atomic ratio variations in F:$AlO_x$ films depending on the weight ratio of FAcAc in the precursors. (b) F 1s, (c) Al 2p, and (d) O 1s XPS of F:$AlO_x$ films with different F content. (e) AFM images of F:$AlO_x$ with different F-doping contents.

observed.[55,59,60] Thus, from Figure 2b–d, it is concluded that F-doping in the present $AlO_x$ films leads to the formation of Al–F bonds likely as an oxyfluoride. GIXRD measurements (Figure S2) indicate that all these F:$AlO_x$ films are essentially amorphous. Moreover, the AFM images (Figure 2e) indicate that all of these films are very smooth although the surface RMS roughness ($\sigma_{RMS}$) increases slightly from 0.21 nm (0–3.7 at. % samples) to 0.22 nm (5.1 at. %) to 0.25 nm (5.9 at. %) due to the formation of some concave–convex spots (diameter of ~150 nm, depth of ~0.8 nm) in the films of 5.1 at. % and 5.9 at. % F:$AlO_x$].

**Dielectric Properties.** Metal–insulator–semiconductor (MIS) capacitors having the structure Au/F:$AlO_x$/Si (Au electrode area = 200 × 200 $\mu m^2$, Figure S3a) were fabricated to characterize the dielectric properties. Leakage current densities versus electrical field ($J$–$E$) of the dielectric films (Figure 3a) indicate that the breakdown electric field of the fluorine-free $AlO_x$ film is 2.7 MV/cm, which agrees with our previous result.[49] The leakage current density at 1.0 MV/cm is ~1.2 × $10^{-7}$ A/$cm^2$ for all the F:$AlO_x$ films, which is comparable to previous reports, indicating excellent insulating properties.[2,17,20] However, upon F-doping, the breakdown electric field increases from 2.7 MV/cm (neat $AlO_x$) to more than 6.0 MV/cm. Especially for the 3.7 at. % F:$AlO_x$ sample, the breakdown electric field reaches 7.0 MV/cm, which is 2.6× times higher than that of neat $AlO_x$ (2.7 MV/cm). Since all films exhibit ostensibly similar morphologies, the increased dielectric strength must originate from differences in $AlO_x$ and F:$AlO_x$ microstructural details.[61,62] This will be discussed further below.

Capacitance–frequency ($C$–$f$) properties were measured in the $10^{-1}$–$10^6$ Hz frequency range under bias voltages of 0, 1, and 2 V (Figures 3b and S3, respectively), with an oscillating voltage of 50 mV. Note that all of these dielectric films were fabricated by combustion synthesis. This procedure was followed, since in preliminary experiments the $C$–$f$ characteristics of pristine $AlO_x$ films fabricated by combustion and conventional sol–gel synthesis (Figure S4) were compared, and although the capacitance instability at lower frequencies, $10^{-1}$–$10^2$ Hz, was identical for all samples, the combustion synthesis-derived films were overall more stable in the $f = 10^{-1}$ Hz → $10^2$ Hz range ($C_{comb}$ = 772 nF/$cm^2$ → 206 nF/$cm^2$, $C_{sol-gel}$ = 1160 nF/$cm^2$ → 276 nF/$cm^2$). This finding is consistent with the general observation that combustion synthesis yields higher quality oxide films than sol–gel for identical processing temperatures.[16,21,63,64]

As shown in Figure 3b, F-doping always enhances capacitance stability versus neat $AlO_x$, especially for $f < 10^2$ Hz. Thus, for a bias of 1 V, the C 1s of the neat $AlO_x$ films rises by more than 7× (from 104 ± 4 nF/$cm^2$ to 781 ± 85 nF/$cm^2$) when $f$ falls from $10^4$ to $10^{-1}$ Hz. The corresponding relative dielectric constant ($\kappa$) approaches 25.5 ± 2.7 and 17.5 ± 1.6 at $10^{-1}$ Hz and 1 Hz, respectively, which are far higher than a typical $AlO_x$ $\kappa$ value of 6–9 (Figure 3c).[1,53] Upon 1.1 at. % F-doping, the capacitance increase for the same frequency range becomes less distinct (from 124 ± 16 nF/$cm^2$ ($10^4$ Hz) to 162 ± 3 nF/$cm^2$ ($10^3$ Hz) to 360 ± 34 nF/$cm^2$ (1 Hz) to 475 ± 50 nF/$cm^2$ ($10^{-1}$ Hz). For the 2.1 at. % sample, the capacitance remains stable (~166 ± 16 nF/$cm^2$) in the frequency range of 1–$10^4$ Hz, while a sharp increase from 207 ± 19 nF/$cm^2$ to 380 ± 40 nF/$cm^2$ occurs when f decreases from 1 to $10^{-1}$ Hz. Note that the $\kappa$ of the 1.1 at. % and 2.1 at. % F:$AlO_x$ films is still not reliable at low frequencies (13.2 ± 1.4 and 9.8 ± 1.0 at $10^{-1}$ Hz for 1.1 at. % and 2.1 at. % F:$AlO_x$, respectively). Importantly, a stable capacitance/$\kappa$ over the entire frequency range is obtained when the F content is increased to 3.7 at. % (166 ± 11 nF/$cm^2$, $\kappa$ = ~4.0). Note that a $\kappa$ of ~4.0 is smaller than that of an ideal $AlO_x$ dielectric, which is usually 8–9. However, since the $\kappa$ of $AlF_3$ is only ~2.2,[65] and F:$AlO_x$ is expected to have a $\kappa$ value somewhere in between that of $AlF_3$ and $AlO_x$.[66] Moreover, F:$AlO_x$ samples with even greater F content (5.1 at. % and 5.9 at. %) exhibit inferior capacitance stability versus 3.7 at. % $AlO_x$ [157 ± 6 nF/$cm^2$ and 160 ± 9 nF/$cm^2$ ($10^4$ Hz) → 371 ± 23 nF/$cm^2$ and 253 ± 7 nF/$cm^2$ ($10^{-1}$ Hz)]. Nevertheless, such 2-fold variations in C 1s are still superior to that of neat $AlO_x$. Note, the capacitances of all F:$AlO_x$ dielectric films decrease at $10^5$ Hz due to the effect of dielectric polarization relaxation.[2] Similar $C$–$f$ trends are obtained for bias voltages of 2 and 0 V (Figure S3b and S3c) although the magnitude of C 1s instability increases with bias. The $\kappa$ values of these F:$AlO_x$ samples are shown in Figure S3d. These results indicate that the mechanism underlying the capacitance instability is related not only to frequency but also to the bias voltage. It is well-known that the capacitance/$\kappa$ of a dielectric material depends on the dielectric polarization mechanism on application of an electric field.[2] In the present neat $AlO_x$ films, it seems that one of the polarizations is only


https://dx.doi.org/10.1021/jacs.0c05161
J. Am. Chem. Soc. 2020, 142, 12440–12452

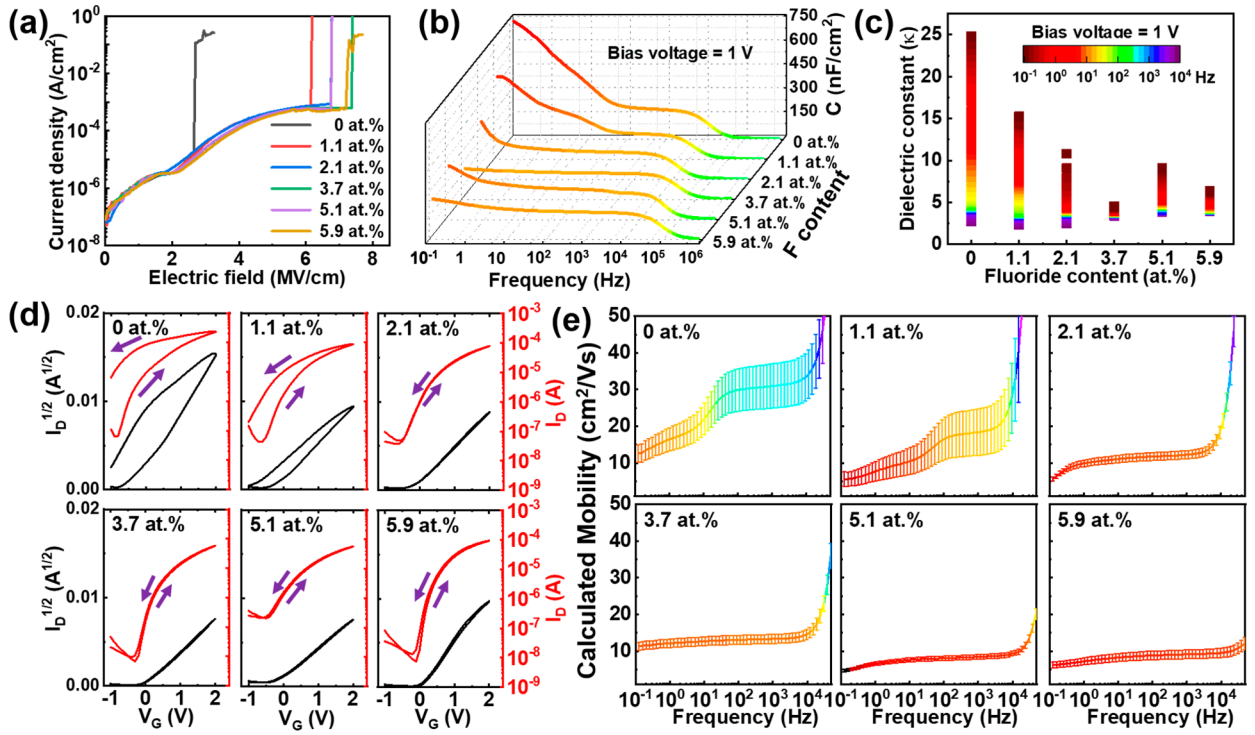


**Figure 3.** (a) Current density−electric field characteristics, (b) capacitance−frequency characteristics of F:$AlO_x$ dielectric films. (c) Corresponding dielectric constant of F:$AlO_x$ films at the indicated frequencies. (d) Representative transfer and (e) calculated mobility−frequency characteristics for the $In_2O_3$ TFTs based on $x$ at.% F:$AlO_x$ dielectric films.

active at frequencies <$10^3$ Hz and F-doping effectively suppresses it. Such a cutoff frequency (~$10^3$ Hz) typically corresponds to electrode and electrode double layer (EDL) polarization, where mobile ions lead to the formation of electric/ionic double layers in/at the electrode/sample interface.[67] Note that this mechanism is in accord with previous proposals that mobile $H^+$ ions in solution-processed $AlO_x$ contribute to the unstable/enlarged capacitance at low frequencies.[34−36]

MIS capacitors based on the 250 °C processed F:$AlO_x$ films were also fabricated to further explore the generality of F-doping and influence of processing temperature. The chemical composition of the 250 °C annealed films was characterized again by XPS, and the data are summarized in Figure S5 and Table S2. The F content in the 250 °C processed F:$AlO_x$ films steadily increases from 0 at. %, to 2.5, 2.8, 3.8, 4.9, and 5.5 at. %, as the FAcAc content of the precursor increases from 0 wt % to 5, 10, 20, 30, and 40 wt %, respectively. Similar to the 300 °C annealed F:$AlO_x$ films, the capacitance stability as a function of frequency improves for an optimal F content (3.8 at. %,Figure S6). At $10^{-1}$ Hz (bias voltage = 2 V), the capacitances of all the films are still higher than those at $10^3$ Hz, 1108, 834, 584, 463, 480, and 562 nF/cm$^2$ at $10^{-1}$ Hz with 0, 2.5, 2.8, 3.8, 4.9, and 5.5 at. % F-doping, respectively, versus ~180 nF/cm$^2$ at $10^3$ Hz for all samples. However, due to the lower processing temperature, the reduced film quality leads to a larger mobile $H^+$ content, enhancing the capacitance dispersion at low frequencies.[34] The 250 and 300 °C annealed films show approximate optimal F content of 3.8 at. % and 3.7 at. %, respectively.

**$In_2O_3$ TFT Performance for Different F:$AlO_x$ Films.** Next, $In_2O_3$ TFTs using F:$AlO_x$ dielectric films (300 °C processing) were fabricated to investigate F-doping effects. Bottom-gate top-contact TFTs (Figure S7a) were fabricated by processing $In_2O_3$ films on Si/F:$AlO_x$ substrates followed by thermal evaporation of Al through a shadow mask for the source/drain electrodes. Fabrication details can be found in the Experimental Section. Figures 3d and S7b show representative transfer and output characteristics, respectively (voltage sweep speed = 0.3 V/s). The devices comprising the neat $AlO_x$ dielectric exhibit significant anticlockwise hysteresis with $\Delta V_{T\text{-}h}$ ($V_T$ shift in hysteresis) as high as 3.2 V. This phenomenon reflects a nonconstant gate capacitance when the device is biased with a continuous $V_G$ sweep from −1 to 2 V, and then back to −1 V. Because of the far higher capacitance at low frequencies under bias (Figure 3b), applying a longer, larger $V_G$ slowly increases the capacitance so that the capacitance is consistently larger in the back-sweep mode. Thus, for the same $V_G$, the drain current ($I_D$) in the back-sweep curve is always higher than that in forward-sweep curve, yielding an anticlockwise hysteresis. However, for 1.1 at. % F-doping, the anticlockwise hysteresis is reduced with a $\Delta V_{T\text{-}h}$ of ~1.2 V. Moreover, the on-current ($I_{on}$, drain current when $V_G = V_D = 2$ V) decreases from $(3.2 \pm 2.3) \times 10^{-4}$ A at 0.0 at. % F to $1.5 \pm 0.9 \times 10^{-4}$ A at 1.1 at. % F. Since F-doping reduces the capacitance at lower frequencies (Figure 3b), a lower $I_D$ is expected. Thus, for the samples with greater F content of 2.1 at. %, and 3.7 at. %,$I_{on}$ continues to fall to $(7.8 \pm 0.9) \times 10^{-5}$ A for 2.1 at. % F and $(5.7 \pm 0.8) \times 10^{-5}$ A for 3.7 at. % F, with a negligible anticlockwise hysteresis, $\Delta V_{T\text{-}h}$ < 0.1 V. Especially for the 3.7 at. % F:$AlO_x$ device, nearly ideal transfer characteristics are obtained, with $V_T$ near 0 V, an on/off ratio of $10^4$, and a small subthreshold swing of 0.2 V/decade (Table S3).

From the $I$−$V$ characteristics, the field effect mobility ($\mu$) is calculated following standard MOSFET equation[2]


https://dx.doi.org/10.1021/jacs.0c05161
J. Am. Chem. Soc. 2020, 142, 12440−12452

Table 1. Electron Mobility ($cm^2/(V\ s)$) as a Function of Frequency for $In_2O_3$ TFTs Having the Indicated F:$AlO_x$ Gate Dielectric Films

| | F content (at. %) | | | | | |
|---|---|---|---|---|---|---|
| Frequency (Hz) | 0 | 1.1 | 2.1 | 3.7 | 5.1 | 5.9 |
| $10^{-1}$ | 11.5 ± 2.2 | 5.4 ± 1.8 | 4.9 ± 0.4 | 11.1 ± 1.0 | 4.6 ± 0.3 | 6.1 ± 0.8 |
| 1 | 16.4 ± 3.2 | 7.8 ± 2.7 | 9.9 ± 0.9 | 12.1 ± 1.1 | 6.6 ± 0.5 | 7.3 ± 1.0 |
| 10 | 22.1 ± 4.3 | 10.6 ± 3.6 | 11.1 ± 1.0 | 12.7 ± 1.2 | 7.6 ± 0.5 | 8.3 ± 1.1 |
| $10^2$ | 30.0 ± 5.8 | 16.7 ± 5.7 | 11.8 ± 1.1 | 13.1 ± 1.2 | 8.1 ± 0.6 | 8.6 ± 1.2 |
| $10^3$ | 31.0 ± 6.0 | 18.4 ± 6.3 | 12.2 ± 1.1 | 13.3 ± 1.2 | 8.4 ± 0.6 | 9.2 ± 1.2 |
| $10^4$ | 34.2 ± 6.6 | 27.7 ± 9.5 | 18.3 ± 1.7 | 14.5 ± 1.4 | 9.4 ± 0.7 | 9.5 ± 1.2 |

$$I_D = (W/2L)\mu C(V_G - V_T)^2 \quad (1)$$

where $C$ is the capacitance per unit area of the dielectric layer, $V_T$ is the threshold voltage, and $V_G$ is gate voltage. $W$ and $L$ are channel width and length, respectively. Since the gate dielectric capacitance is frequency-dependent (Figure 3b), we calculated the frequency dependence of the mobility, and the data are shown in Figure 3e and Table 1. Note, all calculations are based on the forward sweeping curve when the device exhibits hysteresis. Clearly, the calculated mobility−frequency plots demonstrate the pristine $AlO_x$-based TFTs exhibit very large mobility variations with frequency and ranging from 34.2 ± 6.6 $cm^2/(V\ s)$ at $10^4$ Hz to 11.5 ± 2.2 $cm^2/(V\ s)$ for quasi-static ($10^{-1}$ Hz) conditions. Thus, using the high frequency measured capacitance values greatly overestimates the mobility versus that calculated under quasi-static conditions. Upon F-doping the gate dielectric, the calculated mobility range vs $f$ greatly reduces to 27.7 ± 9.5 to 5.4 ± 1.8 $cm^2/(V\ s)$ (1.1 at. % F) and 18.3 ± 1.7 to 4.9 ± 0.4 $cm^2/(V\ s)$ (2.1 at. % F) in the frequency range $10^4$−$10^{-1}$ Hz. Notably, for the 3.7 at. % F:$AlO_x$ TFTs the calculated mobility remains in a narrow range of 14.5 ± 1.4 ($10^4$ Hz) to 11.1 ± 1.0 $cm^2/(V\ s)$ ($10^{-1}$ Hz), with an average value of 12.8 ± 1.1 $cm^2/(V\ s)$. Relatively stable mobilities are also obtained for the devices with the 5.1 at. % and 5.9 at. % F:$AlO_x$, although the absolute values are lower [9.4 ± 0.7 ($10^4$ Hz) to 4.6 ± 0.3 ($10^{-1}$ Hz) $cm^2/(V\ s)$ (5.1 at. % F) and 9.5 ± 1.2 ($10^4$ Hz) to 6.1 ± 0.8 ($10^{-1}$ Hz) $cm^2/(V\ s)$ (5.9 at. % F)] due to the greater trap state densities originating from larger $\sigma_{RMS}$. Therefore, although film uniformity slightly degrades as the F content increases (Figure 2e), the standard deviations of the capacitance and field-effect mobility for the F-doped samples are always lower than those of the pristine $AlO_x$ based devices. Note, the reliable mobility value for the 3.7 at. % F:$AlO_x$ TFTs reflects the stable capacitance characteristics (Figure 3b) enabled by optimal F-doping and good film surface morphology.

**F-doping Effects on F:$AlO_x$ Film Compositional Uniformity, Structure, and Dielectric Response.** To investigate how F-doping enhances the dielectric response, F:$AlO_x$ films were characterized by ToF-SIMS and XPS depth profile. Since it has been suggested that increased capacitance at lower frequencies is due to $H^+$ migration,[36] ToF-SIMS depth profiling was utilized to examine the H and F content in the films. The ToF-SIMS derived F/AlO and H/AlO molar ratios versus the film depth/thickness are shown in Figure 4a. Compared with neat $AlO_x$ films it is found that as the F-doping level increases, the F/AlO ratio gradually increases from ~0.8 to ~9.9 for an etching depth of 5 nm. Note, the $m/z$ values of $F^-$ and $H_3O^-$ overlap, yielding a nonzero value of F/AlO for neat $AlO_x$. In contrast, the H/AlO ratio gradually falls from ~0.7 to ~0.5 at the same etching thickness as the F-doping level increases (Figure 4a). These results indicate that F-doping reduces the $H^+$ content in F:$AlO_x$ films. Interestingly, as the etching depth is increased from 0 to 20 nm, all element contents slightly decrease. A similar result is found for the XPS depth profile (Figure S8), which may be due to the imperfect dielectric film etching in ToF-SIMS and XPS processes.[68]

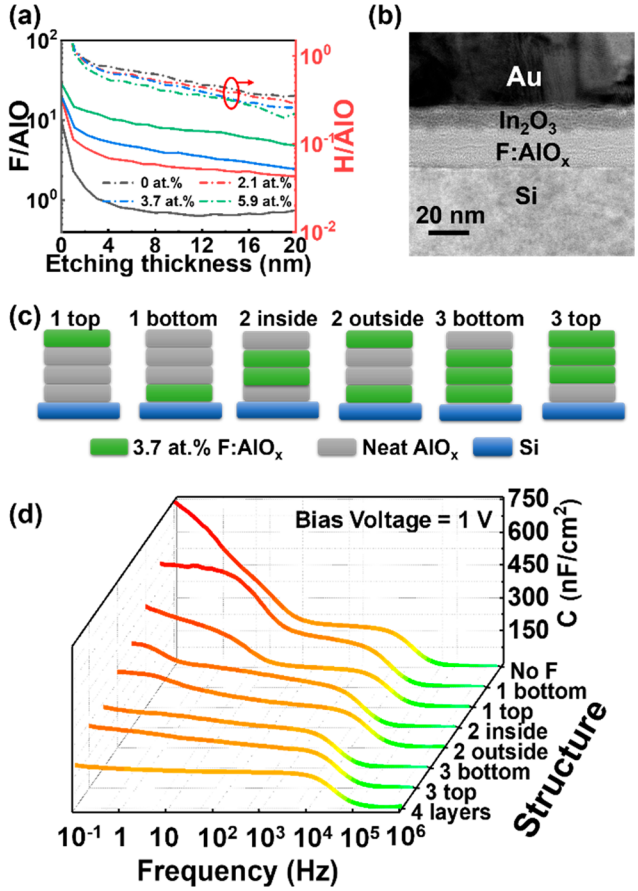


Figure 4. (a) ToF-SIMS as a function of F content for F:$AlO_x$ films and (b) cross-section TEM of a 3.7 at. % F:$AlO_x$ film along with an $In_2O_3$ film. (c) Structures of $AlO_x$ dielectrics with different 3.7 at. % F-doped layers. (d) Capacitance−frequency characteristics of four-layer $AlO_x$ films with different number and location of 3.7 at. % F-doped layers.

Next, cross-sectional Transmission Electron Microscopy (TEM) was carried out on a multilayer consisting of the same 3.7 at. % F:$AlO_x$ film on Si/$SiO_x$ coated with an $In_2O_3$ film and then with an additional protective gold film (Figures 4b and S9). Note that the F:$AlO_x$ and $In_2O_3$ solution film growth processes are identical to those used for TFTs. These images reveal well-defined $In_2O_3$/F:$AlO_x$ and F:$AlO_x$/Si


https://dx.doi.org/10.1021/jacs.0c05161
J. Am. Chem. Soc. 2020, 142, 12440−12452

interfaces, where the Si substrate is a single crystal, the F:$AlO_x$ is amorphous, and the $In_2O_3$ is polycrystalline. The corresponding energy dispersive X-ray spectroscopy (EDS) of In, Al, Si, O, Au, and F elemental mapping was also conducted as shown in Figure S9, evidencing no obvious interlayer diffusion which further proves the optimal interlayer structure in our transistors. Note that F-mapping is not informative here due to the beam damage during the sample preparation process (focused ion beam, FIB).

In addition, since the present dielectric films are composed of four F:$AlO_x$ layers, and each layer is about 5 nm thick (*vide supra*), it is possible to inquire whether the effect of F-doping on the overall dielectric response is primarily bulk- or interface-dominated by fabricating mixed F-doped and undoped multilayer structures as shown in Figure 4c. Here a doping level of 3.7 at. % F is employed, since it corresponds, for the fully 4-layer doped multilayer, to the best-performing F:$AlO_x$ dielectric film. Capacitance versus frequency characteristics of these mixed F-doped films are shown in Figures 4d and S10. Compared with the neat $AlO_x$ films, the $C$–$f$ plots of Figure 4d clearly demonstrate that F-doping only the top $AlO_x$ layer, in contact with the TFT channel, or only the inner layers, does not suppress C variations. That is, F must be incorporated in all four layers to optimize the dielectric response of these films, further supporting the mechanism of (bulk) $H^+$ migration as the source of C dispersion.

**F:$AlO_x$ NMR and Optical Characterization.** Multinuclear ($^{19}F$, $^{27}Al$, and $^{1}H$) solid-state magic-angle-spinning (MAS) NMR was employed to understand $AlO_x$ structure upon fluoride incorporation. $^{19}F$ NMR corroborates successful F-incorporation in the F:$AlO_x$ samples. As shown in Figure 5a (detailed analysis in Figures 5b and S11a), the main peak centered at about −130 ppm represents the oxyfluoride phase,[69] in particular, $AlO_3F_3$. Minor peaks from impurities (∼−60 ppm) and the chemical environment surrounding the F changes [e.g., Al−F−Al; (changes in bond length) to Al−F−(vacancy)] when the F content varies from 1.1 at. % to 3.7 at. % (Figure S11b).[70−72] Furthermore, the $^{19}F$ NMR peak area integration reveals that almost 90% of F-containing species are oxyfluoride (Figures 5c and S11c).

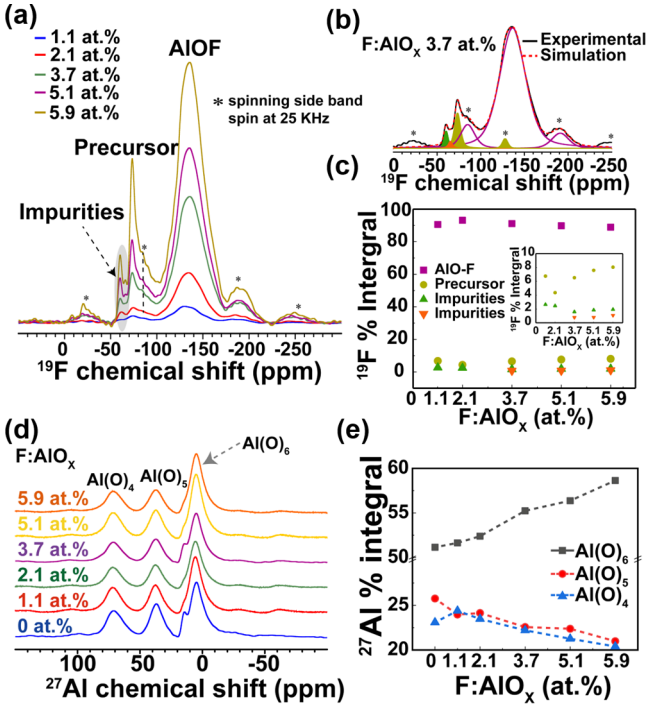


**Figure 5.** (a) Solid-state $^{19}F$ MAS NMR of the indicated F:$AlO_x$ samples. (b) Representative spectral analysis of the $^{19}F$ NMR. (c) Quantification by area integral of the resonances normalized relative to the $^{19}F$ NMR fraction of the 5.9 at. % sample. (d) $^{27}Al$ NMR of the indicated F:$AlO_x$ samples. (e) Fraction of $Al(O)_4$, $Al(O)_5$ and $Al(O)_6$ coordination environments based on $^{27}Al$ NMR spectra in (d).

The $^{27}Al$ and $^{1}H$ NMR was also utilized to examine the aluminum and hydrogen environments in these samples. The $^{27}Al$ NMR spectra exhibit three resonances corresponding to the various coordination environments as shown in Figure 5d. Tetrahedral, pentahedral, and octahedral Al coordination are observed at ∼76, 37, and 6 ppm, respectively.[73] Fluoride incorporation increases the peak intensity of the octahedral coordination as shown in Figure 5e. This implies that fluoride prefers to be associated with Al in the octahedra coordination in the form of $AlO_3F_3$. Upon increasing the F content, the percentage of $Al(O)_6$ increases from 52.1% (0 at. % F) to 58.6% (5.9 at. % F) and the percentage of $Al(O)_4$ decreases from 23.1% (0 at. % F) to 20.4% (5.9 at. % F). The conversion of $Al(O)_4$ and $Al(O)_5$ to $Al(O)_6$ species is known to suppress ionic polarization and suppress dielectric constant dispersion with frequency in conventional dielectric materials.[74] According to previous studies, mobile $H^+$ ions contribute to slow polarization originating from slow formation of dipole moments in solution processed oxide dielectrics in bulk of dielectric films.[34,40] Here the increased percentage of $Al(O)_6$ indicates that F-doping reduces the concentration and the effect of $H^+$ migration, thereby enhancing capacitance stability at low frequency. In addition, the $Al(O)_5$ structure usually surrounds an oxygen vacancy, which is known to create defects in dielectric films.[75,76] Thus, decreasing the $Al(O)_5$ content with F-doping reduces defects, which thus stabilizes dielectric response. Note that the acidity of $Al(O)_4$ is much greater than $Al(O)_6$,[77] further supporting that their diminution upon F incorporation will reduce the F:$AlO_x$ dielectric film acidity. This should thus decrease O−H ionization producing $H^+$ ions.

Finally, $^{1}H$ NMR spectra show the presence of three resonances at ∼2, ∼5, and ∼8 ppm, which are assigned as terminal OH, double bridged OH, and triple bridged OH, respectively (Figure S12a and S12b).[78−80] Upon fluorination, the percentage of the terminal OH is reduced while the double and triple bridged OH resonances increase (Figure S12c and S12d). Combined with the $^{27}Al$ NMR results, the conversion of $Al(O)_4$ and $Al(O)_5$ species to $Al(O)_6$ sites with bridged hydroxide ligands should increase the Al coordination numbers which should minimize the frequency dependence of the dielectric properties.[74]

Next, UV−vis absorption measurements on the F:$AlO_x$ films were carried out, and the optical band gaps calculated from the data in Figure S13. Note that the small peak ∼5.3 eV in Figure S13 is due to the absorption from the quartz substrate. From a Tauc's plot analysis, it can be seen that the F:$AlO_x$ film band gap enlarges ($E_g$ = 5.74 eV → 5.81 eV → 5.82 eV → 5.85 eV → 5.86 eV → 5.87 eV) as the F-doping content increases in the progression, F content = 0 at. % → 1.1 at. % → 2.1 at. % → 3.7 at. % → 5.1 at. % → 5.9 at. %. This is because the potential of F 2p orbitals is deeper than that of O 2p orbitals. And this result is consistent with the far larger band gap of $AlF_3$ films deposited by physical vapor deposition (∼10.8 eV) versus $Al_2O_3$ (∼6.7 eV)[81] and supports formation of Al−F bonds


https://dx.doi.org/10.1021/jacs.0c05161
J. Am. Chem. Soc. 2020, 142, 12440−12452

identified in the NMR spectra, and thus formation of oxyfluorides. Note that for a dielectric material, a larger band gap usually correlates with a lower dielectric constant[82−84] (specifically $\kappa_{Al_2O_3}$ = ∼9; $\kappa_{AlF_3}$ = 2.2); these data are also consistent with the dielectric constant trends reported in Figure 3c, where $\kappa$ falls as the F content increases from 0.0 at. % to 5.9 at. %.

**Fluoride Sources for Combustion Synthesis of F:AlO$_x$ Films.** To probe whether other F sources can be used in the present growth process, two other fluoro-organic reagents were investigated, specifically, FMEK and MFAcAc chemical structures in Figure 1a. Both molecules have similar C−F bonds and chelating capacity as FAcAc. Thermogravimetry and differential scanning calorimetry (TGA/DSC) measurements were conducted (Figure S14a and S14b) and indicate that all the precursors exhibit typical combustion process behavior with obvious exothermal peaks. The goal was to grow F:AlO$_x$ films following similar procedures for ∼3.7 at. % F content since this composition affords the most stable dielectric response when FAcAc is the F source. Unfortunately, after several trials (not shown), we were unable to achieve F-doped AlO$_x$ films using FMEK (assessed by XPS) likely reflecting the low FMEK boiling point, ∼51 °C (Figure S14c). However, with a 25 wt % vs Al(NO$_3$)$_3$ of MFAcAc as the precursor solution F source, ∼3.7 at. % F:AlO$_x$ films were achieved. Moreover, the $C$−$f$ characteristics in Figure S14d demonstrate superior response compared to those of AlO$_x$ films; however, the capacitance is not as stable as those grown with FAcAc. XRR scans were performed on the F:AlO$_x$ layer (Figure S15a), and fitted film XRR electron-density profiles are shown in Figure S15b. The fitting shows that the densities of neat AlO$_x$, 3.7 at. % doped F:AlO$_x$ with FAcAc and MFAcAc films are 0.89, 0.88, and ·0.79 eÅ$^{-3}$, respectively. This indicates that the FAcAc-derived films are significantly denser than those from MFAcAc, in agreement with the corresponding dielectric metrics.[49] Thus, FAcAc remains the reagent of choice for fluoride doping of AlO$_x$ dielectric films.

**Applicability to Organic Transistors.** To demonstrate the general applicability of the F:AlO$_x$ gate dielectric films, TFTs were fabricated using organic p-type semiconductors P5 (vacuum grown small molecule), TIPS-P5 (solution-processed small molecule), and DPP-DTT (solution-processed polymer) shown in Figures 6a, to complement inorganic In$_2$O$_3$ (Figure S16a and S16b). In comparison to In$_2$O$_3$ TFT performance, strikingly similar behavior is observed in the transfer characteristics of P5 TFTs (Figure 6b and Table S4).

An obvious clockwise hysteresis [$\Delta V_{T\text{-}h}$ = 0.3 V; see SI for details] is observed for all AlO$_x$-based P5 TFTs while the 1.1 at. % and 3.7 at. % F:AlO$_x$ devices exhibit negligible hysteresis ($\Delta V_{T\text{-}h}$ < 0.01 V). As the F content is increased further (5.9 at. % F), an anticlockwise hysteresis is observed (back-sweeping current falls <0.75× versus the forward-sweeping current). This phenomenon is due to the relatively large trap density at the pentacene/dielectric interface.[85−87] From the $C$−$f$ characteristics, the calculated mobility−$f$ characteristics of these pentacene TFTs are plotted in Figures 6c and S17, and the results are summarized in Table S5. Similar to the In$_2$O$_3$ TFTs, the P5/AlO$_x$ TFTs exhibit a large variation in extracted mobility, from 0.04 cm$^2$/(V s) to 0.25 cm$^2$/(V s), with frequency ($10^{-1}$−$10^4$ Hz), while F-doping of the dielectric greatly stabilizes the mobility over a wide frequency range.

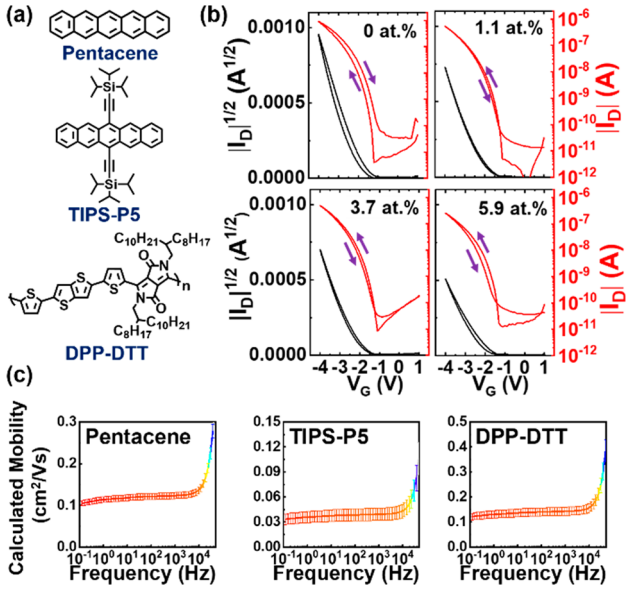


**Figure 6.** (a) Molecular structures of pentacene, TIPS-P5 and DPP-DTT. (b) Representative transfer plots of pentacene TFTs based on the indicated F:AlO$_x$ gate dielectric films. (c) and calculated mobility−frequency characteristics based on 3.7 at. % F:AlO$_x$ dielectric film.

Especially for the 3.7 at. % F:AlO$_x$ devices, the mobility is stable at 0.12 ± 0.01 cm$^2$/(V s).

Next, the optimal 3.7 at. % F:AlO$_x$ film composition was used to expand the use scope of this dielectric to TIPS-P5 and DPP-DTT TFTs. Similar mobility behavior is obtained for these devices (Figures 6c and S18). The mobilities of TIPS-P5 and DPP-DTT TFTs remain at 0.035 ± 0.004 cm$^2$/(V s) and 0.13 ± 0.01 cm$^2$/(V s), respectively, for a 0.1 to $10^4$ Hz frequency range. These results clearly show that an optimal amount of F-doping into the AlO$_x$ dielectric enhances the stability of both organic and inorganic, as well as n- and p-type, transistor characteristics to afford reliable mobilities.

**Understanding the Bias-Stress Stability of Oxide vs Organic Transistors.** Gate bias stability tests of In$_2$O$_3$-based TFTs and P5-based TFTs with different dielectric compositions were conducted to assess how F-doped AlO$_x$ TFTs behave under this important performance evaluation and compare it to the static $I$−$V$ characteristics shown above. The results in terms of $I_{on}$ and $V_T$ variations, $|\Delta I_{on}|$ and $\Delta V_{T\text{-}b}$ ($V_T$ shift in bias-stress), are shown in Figure 7a and 7b, respectively, while Figure 7c reports the $I$−$V$ hysteresis in static conditions ($\Delta V_{T\text{-}h}$) extracted from Figures 3d (for In$_2$O$_3$) and 6b (for P5).

For the In$_2$O$_3$-based TFTs, $I_{on}$ was monitored for 500 s with $V_G$ = $V_D$ = +2.0 V at 22 °C (Figure S19a). Thus, $I_{on}$ of the TFTs using 0.0 at. % and 1.1 at. % F:AlO$_x$ increases from 0.25 mA and 0.15 mA (0 s) to 0.91 mA and 0.53 mA (500 s), respectively, during the bias stress test. $I_{on}$ increases more than 3.5× over the original value, indicating that the capacitance rises when the gate bias is applied. This is also evident when the TFT transfer curves measured before and after 500s gate bias are compared (Figure S19b). The transfer curves of both the 0.0 at. % and 1.1 at. % F:AlO$_x$ devices shift significantly to negative biases and, thus, cannot be turned off, resulting in "open channel" behavior. This corresponds to $V_T$ shifting from −1.5 V and −0.4 V (0s) to −9.0 V and −3.2 V (500 s), thus a $\Delta V_{T\text{-}b}$ of −7.5 V and −2.8 V, respectively. These results are


https://dx.doi.org/10.1021/jacs.0c05161
J. Am. Chem. Soc. 2020, 142, 12440−12452

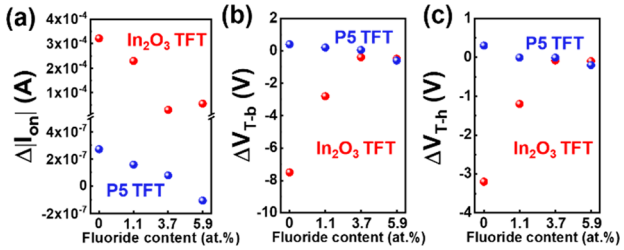


**Figure 7.** Variation of $I_{on}$ (a) and $V_{T\text{-}b}$ (b) acquired from TFT transfer curves measured before and after 500 s gate bias. (c) The $I$–$V$ hysteresis of $\Delta V_{T\text{-}h}$, which get from the transfer curves in Figures 3d and 6b.

consistent with the $C$–$f$ characteristics, with an enhanced capacitance at low frequencies and thus unstable device response. However, for the 3.7 at. % F:$AlO_x$ devices, $I_{on}$ is far more stable, only increasing from 0.03 mA (0 s) to 0.05 mA (500 s), with a $\Delta V_{T\text{-}b}$ of only −0.4 V. A similar phenomenon is observed for the 5.9 at. % F:$AlO_x$ devices, $I_{on}$: 0.10 mA (0 s) → 0.18 mA (500 s), $V_T$: −0.1 V (0 s) → −0.6 V (500 s); thus, this sample is also for more stable than the neat $AlO_x$ devices. Note that these results are in contrast to a general bias-stress stability test trend in $In_2O_3$ TFTs based on a $SiO_2$ gate dielectric[88,89] (Figure S20a and S20b), where $I_{on}$ monotonically decreases from 3.82 mA (0.0 s) to 0.52 mA (500 s), with a positive $V_T$ shift from 2 V (0.0 s) to 18 V (500 s). These results can be understood to be a consequence of $H^+$ motion toward the semiconductor interface in the gate electric field.[35] This accumulates $H^+$ in the dielectric and electrons in the $In_2O_3$ side of the F:$AlO_x$/$In_2O_3$ interface, forming an electrical double layer (EDL), increasing the areal capacitance under stress, and thus enhancing $I_{on}$ and shifting $V_{T\text{-}b}$ to negative biases.[35,36] The $I_{on}$ enhancement for the 3.7 at. % F:$AlO_x$ sample is negligible versus that of neat $AlO_x$, showing that F-doping of the gate dielectric effectively reduces mobile $H^+$ effects, as confirmed from the dielectric chemical and structural analysis above. This result is also consistent with the large counterclockwise $I$–$V$ hysteresis in the $In_2O_3$-based TFT transfer curves (Figure 3d), which is greatly suppressed from 0.0 at. % F:$AlO_x$ ($\Delta V_{T\text{-}h}$ = −3.2 V) to the 3.7 at. % F:$AlO_x$ ($\Delta V_{T\text{-}h}$ = −0.08 V).

For the P5 TFT gate bias stress test, $I_{on}$ was monitored for 500 s with $V_G$ = $V_D$ = −4.0 V (Figure S21a and S21b). Both the 0.0 at. % and 1.1 at. % F:$AlO_x$ devices exhibit similar $I_{on}$ trends to the $In_2O_3$ TFTs, with the $I_{on}$'s increasing from 0.26 μA and 0.20 μA (0 s) to 0.68 μA and 0.50 μA (500s), respectively. However, these variations are remarkably lower than those of the $In_2O_3$ TFTs. Furthermore, $V_T$ shifts from −2.1 V and −2.3 V (0 s) to −1.7 V and −2.1 V (500 s), yielding a $\Delta V_{T\text{-}b}$ of +0.4 V and +0.2 V, respectively for these devices. Interestingly, for the 3.7 at. % F:$AlO_x$ TFTs, $I_{on}$ first falls slightly, from 0.24 μA (0 s) to 0.23 μA (50 s) followed by a slow increase to 0.34 μA after 500 s, so again $I_{on}$ is far more stable than that for neat $AlO_x$ TFTs. In 3.7 at. % F:$AlO_x$ TFT, $V_T$ shifts from −2.20 V (0 s) to −2.15 V (500 s), and thus $\Delta V_{T\text{-}b}$ is only +0.05 V. However, for 5.9 at. % F:$AlO_x$ TFTs, $I_{on}$ falls substantially with time from 0.16 μA to 0.06 μA, while $\Delta V_{T\text{-}b}$ increases to −0.6 V ($V_T$ = −2.4 V to −3.0 V), which is ascribable to the considerable trap accumulation at the pentacene/dielectric interface.[86,87] Regarding hysteresis, $\Delta V_{T\text{-}h}$ of neat $AlO_x$ P5-based TFTs is clockwise and +0.3 V, considerably smaller than that of the $AlO_x$/$In_2O_3$ TFT (−3.2 V; Figure 7c). Upon F-doping the dielectric $\Delta V_{T\text{-}h}$ becomes anticlockwise and first decreases considerably to ∼−0.01 V for the 1.1 at. % and 3.7 at. % samples and then increases to −0.2 V for the 5.9 at. % F:$AlO_x$/P5 devices. The 3.7 at. % F:$AlO_x$ sample has the smallest $I_{on}$ variation and $V_{T\text{-}b}$ shift under the gate bias stress, meaning that mobile $H^+$ ions are effectively eliminated in the F:$AlO_x$ dielectric. Furthermore, for the P5-based TFTs, the variation of $I_{on}$ and $V_T$ is less than in $In_2O_3$ TFTs, reflecting the effects of enhanced capacitance in the dielectric eliminating the trap effects at the P5/F:$AlO_x$ interface. These bias-stress stability evaluations of $In_2O_3$ and P5 TFTs confirm that excellent $AlO_x$ dielectrics can be created by solution phase low-temperature fluoride doping.

## CONCLUSIONS

An expeditious, tunable approach is reported to enhance the capacitance stability of high-κ $AlO_x$ dielectrics over a broad frequency range via fluoride doping. Using an optimal F:$AlO_x$ composition as the gate dielectric, both inorganic and organic semiconductor TFTs exhibit reliable carrier mobility behavior and negligible $I$–$V$ hysteresis. The enhanced capacitance stability and excellent TFT performance originate from reducing the $H^+$ content and mobility as assessed by multiple physical techniques. This work demonstrates that anion doping of metal oxides is broad in scope and opens a new means to fabricate reliable and high performance TFTs via solution processing at low temperatures, as well as the correct interpretation of their performance characteristics. We believe that the concept demonstrated here for metal oxide transistors should be applicable to the development of new low temperature functional oxide materials for a wide range of applications in optoelectronics, energy storage, and energy conversion.

## ASSOCIATED CONTENT

### Supporting Information

The Supporting Information is available free of charge at https://pubs.acs.org/doi/10.1021/jacs.0c05161.

Detailed schematic of F:AlOx film fabrication process, XPS of F:$AlO_x$, atomic ratio in F:$AlO_x$, XRD of F:$AlO_x$, capacitance and calculated dielectric constant of F:$AlO_x$, output characteristics bias-stress stability and parameter of TFT, HAADF-STEM, solid-state NMR, UV–vis absorption, and XRR (PDF)

## AUTHOR INFORMATION

### Corresponding Authors

**Vinayak P. Dravid** − *Department of Materials Science and Engineering, The NUANCE Center, Northwestern University, Evanston, Illinois 60208, United States;* orcid.org/0000-0002-6007-3063; Email: v-dravid@northwestern.edu

**Junsheng Yu** − *State Key Laboratory of Electronic Thin Films and Integrated Devices, School of Optoelectronic Science and Technology, University of Electronic Science and Technology of China (UESTC), Chengdu 610054, China;* orcid.org/0000-0002-7484-8114; Email: jsyu@uestc.edu.cn

**Yan-Yan Hu** − *Center of Interdisciplinary Magnetic Resonance, National High Magnetic Field Laboratory, Tallahassee, Florida 32310, United States; Department of Chemistry and Biochemistry, Florida State University, Tallahassee, Florida 32306, United States;* Email: yhu@fsu.edu



https://dx.doi.org/10.1021/jacs.0c05161
J. Am. Chem. Soc. 2020, 142, 12440−12452

**Wei Huang** − *Department of Chemistry and the Materials Research Center, Northwestern University, Evanston, Illinois 60208, United States;* orcid.org/0000-0002-0973-8015; Email: weihuang@northwestern.edu

**Antonio Facchetti** − *Department of Chemistry and the Materials Research Center, Northwestern University, Evanston, Illinois 60208, United States; Flexterra Corporation, Skokie, Illinois 60077, United States;* orcid.org/0000-0002-8175-7958; Email: a-facchetti@northwestern.edu

**Tobin J. Marks** − *Department of Chemistry and the Materials Research Center, Northwestern University, Evanston, Illinois 60208, United States;* orcid.org/0000-0001-8771-0141; Email: t-marks@northwestern.edu

### Authors

**Xinming Zhuang** − *State Key Laboratory of Electronic Thin Films and Integrated Devices, School of Optoelectronic Science and Technology, University of Electronic Science and Technology of China (UESTC), Chengdu 610054, China; Department of Chemistry and the Materials Research Center, Northwestern University, Evanston, Illinois 60208, United States*

**Sawankumar Patel** − *Department of Chemistry and Biochemistry, Florida State University, Tallahassee, Florida 32306, United States*

**Chi Zhang** − *Department of Materials Science and Engineering, The NUANCE Center, Northwestern University, Evanston, Illinois 60208, United States*

**Binghao Wang** − *Department of Chemistry and the Materials Research Center, Northwestern University, Evanston, Illinois 60208, United States;* orcid.org/0000-0002-9631-6901

**Yao Chen** − *Department of Chemistry and the Materials Research Center, Northwestern University, Evanston, Illinois 60208, United States;* orcid.org/0000-0003-4414-8528

**Haoyu Liu** − *Department of Chemistry and Biochemistry, Florida State University, Tallahassee, Florida 32306, United States*

Complete contact information is available at: https://pubs.acs.org/10.1021/jacs.0c05161

### Notes

The authors declare no competing financial interest.

## ■ ACKNOWLEDGMENTS

We thank the US-Israel Binational Science Foundation (Grant AGMT-2012250///02), the Northwestern University Materials Research Science and Engineering Center (MRSEC NSF Grant DMR-1720139), the Air Force Office of Scientific Research (Grant FA9550-18-1-0320), and Flexterra Corporation for support of this research. This work made use of the J. B. Cohen X-ray Diffraction Facility, Northwestern University Micro/Nano Fabrication Facility (NUFAB), EPIC facility, Keck-II facility, and SPID facility of the NUANCE Center at Northwestern University, which is partially supported by the Soft and Hybrid Nanotechnology Experimental (SHyNE) Resource (NSF ECCS-1542205), the Materials Research Science and Engineering Center (DMR-1720139), the State of Illinois, and Northwestern University. All solid-sate NMR experiments were performed at the National High Magnetic Field Laboratory. The National High Magnetic Field Laboratory is supported by National Science Foundation through Grant NSF/DMR-1644779 and the State of Florida. J.Y. thanks the National Key R&D Program of China (Grant No. 2018YFB0407102), the Foundation of National Natural Science Foundation of China (NSFC) (Grant Nos. 61421002, 61675041, and 51703019), and Sichuan Science and Technology Program (Grant Nos. 2019YFH0005, 2019YFG0121, and 2019YJ0178) for support (synthesis and characterization). X.Z. thanks the joint-Ph.D. program supported by the China Scholarship Council (No. 201806070112) for a fellowship.

## ■ REFERENCES

(1) Liu, A.; Zhu, H.; Sun, H.; Xu, Y.; Noh, Y. Y. Solution Processed Metal Oxide High-k Dielectrics for Emerging Transistors and Circuits. *Adv. Mater.* **2018**, *30*, 1706364.

(2) Wang, B.; Huang, W.; Chi, L.; Al-Hashimi, M.; Marks, T. J.; Facchetti, A. High- k Gate Dielectrics for Emerging Flexible and Stretchable Electronics. *Chem. Rev.* **2018**, *118*, 5690−5754.

(3) Daunis, T. B.; Schroder, K. A.; Hsu, J. W. P. Photonic curing of solution-deposited ZrO2 dielectric on PEN: a path towards high-throughput processing of oxide electronics. *npj Flex. Electron.* **2020**, *4*, 7.

(4) Carey, B. J.; Ou, J. Z.; Clark, R. M.; Berean, K. J.; Zavabeti, A.; Chesman, A. S.; Russo, S. P.; Lau, D. W.; Xu, Z. Q.; Bao, Q.; Kevehei, O.; Gibson, B. C.; Dickey, M. D.; Kaner, R. B.; Daeneke, T.; Kalantar-Zadeh, K. Wafer-scale two-dimensional semiconductors from printed oxide skin of liquid metals. *Nat. Commun.* **2017**, *8*, 14482.

(5) Heo, J.; Park, S. Y.; Kim, J. W.; Song, S.; Yoon, Y. J.; Jeong, J.; Jang, H.; Lee, K. T.; Seo, J. H.; Walker, B.; Kim, J. Y. Implementation of Low-Power Electronic Devices Using Solution-Processed Tantalum Pentoxide Dielectric. *Adv. Funct. Mater.* **2018**, *28*, 1704215.

(6) Huang, W.; Zeng, L.; Yu, X.; Guo, P.; Wang, B.; Ma, Q.; Chang, R. P. H.; Yu, J.; Bedzyk, M. J.; Marks, T. J.; Facchetti, A. Metal Oxide Transistors via Polyethylenimine Doping of the Channel Layer: Interplay of Doping, Microstructure, and Charge Transport. *Adv. Funct. Mater.* **2016**, *26*, 6179−6187.

(7) Ginley, D. S.; Bright, C. Transparent Conducting Oxides. *MRS Bull.* **2000**, *25*, 15−18.

(8) Chen, Y.; Huang, W.; Sangwan, V. K.; Wang, B.; Zeng, L.; Wang, G.; Huang, Y.; Lu, Z.; Bedzyk, M. J.; Hersam, M. C.; Marks, T. J.; Facchetti, A. Polymer Doping Enables a Two-Dimensional Electron Gas for High-Performance Homojunction Oxide Thin-Film Transistors. *Adv. Mater.* **2019**, *31*, 1805082.

(9) Lee, H. E.; Kim, S.; Ko, J.; Yeom, H.-I.; Byun, C.-W.; Lee, S. H.; Joe, D. J.; Im, T.-H.; Park, S.-H. K.; Lee, K. J. Skin-Like Oxide Thin-Film Transistors for Transparent Displays. *Adv. Funct. Mater.* **2016**, *26*, 6170−6178.

(10) Petti, L.; Münzenrieder, N.; Vogt, C.; Faber, H.; Büthe, L.; Cantarella, G.; Bottacchi, F.; Anthopoulos, T. D.; Tröster, G. Metal oxide semiconductor thin-film transistors for flexible electronics. *Appl. Phys. Rev.* **2016**, *3*, No. 021303.

(11) Park, B.; Ho, D.; Kwon, G.; Kim, D.; Seo, S. Y.; Kim, C.; Kim, M.-G. Solution-Processed Rad-Hard Amorphous Metal-Oxide Thin-Film Transistors. *Adv. Funct. Mater.* **2018**, *28*, 1802717.

(12) Yu, X.; Marks, T. J.; Facchetti, A. Metal oxides for optoelectronic applications. *Nat. Mater.* **2016**, *15*, 383−396.

(13) Kwon, G.; Kim, K.; Choi, B. D.; Roh, J.; Lee, C.; Noh, Y. Y.; Seo, S.; Kim, M. G.; Kim, C. Multifunctional Organic-Semiconductor Interfacial Layers for Solution-Processed Oxide-Semiconductor Thin-Film Transistor. *Adv. Mater.* **2017**, *29*, 1607055.

(14) White, M. S.; Olson, D. C.; Shaheen, S. E.; Kopidakis, N.; Ginley, D. S. Inverted bulk-heterojunction organic photovoltaic device using a solution-derived ZnO underlayer. *Appl. Phys. Lett.* **2006**, *89*, 143517.

(15) Huang, W.; Guo, P.; Zeng, L.; Li, R.; Wang, B.; Wang, G.; Zhang, X.; Chang, R. P. H.; Yu, J.; Bedzyk, M. J.; Marks, T. J.; Facchetti, A. Metal Composition and Polyethylenimine Doping Capacity Effects on Semiconducting Metal Oxide-Polymer Blend Charge Transport. *J. Am. Chem. Soc.* **2018**, *140*, 5457−5473.

(16) Kim, M. G.; Kanatzidis, M. G.; Facchetti, A.; Marks, T. J. Low-temperature fabrication of high-performance metal oxide thin-film

electronics via combustion processing. *Nat. Mater.* **2011**, *10*, 382−388.
(17) Wang, B.; Yu, X.; Guo, P.; Huang, W.; Zeng, L.; Zhou, N.; Chi, L.; Bedzyk, M. J.; Chang, R. P. H.; Marks, T. J.; Facchetti, A. Solution-Processed All-Oxide Transparent High-Performance Transistors Fabricated by Spray-Combustion Synthesis. *Adv. Electron. Mater.* **2016**, *2*, 1500427.
(18) Banger, K. K.; Yamashita, Y.; Mori, K.; Peterson, R. L.; Leedham, T.; Rickard, J.; Sirringhaus, H. Low-temperature, high-performance solution-processed metal oxide thin-film transistors formed by a 'sol-gel on chip' process. *Nat. Mater.* **2011**, *10*, 45−50.
(19) Lin, Y. H.; Faber, H.; Zhao, K.; Wang, Q.; Amassian, A.; McLachlan, M.; Anthopoulos, T. D. High-performance ZnO transistors processed via an aqueous carbon-free metal oxide precursor route at temperatures between 80−180 degrees C. *Adv. Mater.* **2013**, *25*, 4340−4346.
(20) Scheideler, W. J.; McPhail, M. W.; Kumar, R.; Smith, J.; Subramanian, V. Scalable, High-Performance Printed InO x Transistors Enabled by Ultraviolet-Annealed Printed High- k AlO x Gate Dielectrics. *ACS Appl. Mater. Interfaces* **2018**, *10*, 37277−37286.
(21) Yu, X.; Smith, J.; Zhou, N.; Zeng, L.; Guo, P.; Xia, Y.; Alvarez, A.; Aghion, S.; Lin, H.; Yu, J.; Chang, R. P.; Bedzyk, M. J.; Ferragut, R.; Marks, T. J.; Facchetti, A. Spray-combustion synthesis: efficient solution route to high-performance oxide transistors. *Proc. Natl. Acad. Sci. U. S. A.* **2015**, *112*, 3217−3222.
(22) Liang, Y.; Yong, J.; Yu, Y.; Nirmalathas, A.; Ganesan, K.; Evans, R.; Nasr, B.; Skafidas, E. Direct Electrohydrodynamic Patterning of High-Performance All Metal Oxide Thin-Film Electronics. *ACS Nano* **2019**, *13* (12), 13957−13964.
(23) Garlapati, S. K.; Divya, M.; Breitung, B.; Kruk, R.; Hahn, H.; Dasgupta, S. Printed Electronics Based on Inorganic Semiconductors: From Processes and Materials to Devices. *Adv. Mater.* **2018**, *30*, 1707600.
(24) Xu, W.; Long, M.; Zhang, T.; Liang, L.; Cao, H.; Zhu, D.; Xu, J.-B. Fully solution-processed metal oxide thin-film transistors via a low-temperature aqueous route. *Ceram. Int.* **2017**, *43*, 6130−6137.
(25) Carlos, E.; Branquinho, R.; Kiazadeh, A.; Martins, J.; Barquinha, P.; Martins, R.; Fortunato, E. Boosting Electrical Performance of High-kappa Nanomultilayer Dielectrics and Electronic Devices by Combining Solution Combustion Synthesis and UV Irradiation. *ACS Appl. Mater. Interfaces* **2017**, *9*, 40428−40437.
(26) Jang, J.; Kitsomboonloha, R.; Swisher, S. L.; Park, E. S.; Kang, H.; Subramanian, V. Transparent high-performance thin film transistors from solution-processed $SnO_2$ /$ZrO_2$ gel-like precursors. *Adv. Mater.* **2013**, *25*, 1042−1047.
(27) Liu, A.; Liu, G. X.; Zhu, H. H.; Xu, F.; Fortunato, E.; Martins, R.; Shan, F. K. Fully solution-processed low-voltage aqueous In2O3 thin-film transistors using an ultrathin $ZrO_{(x)}$ dielectric. *ACS Appl. Mater. Interfaces* **2014**, *6*, 17364−17369.
(28) Xu, W.; Wang, H.; Ye, L.; Xu, J. The role of solution-processed high-$\kappa$ gate dielectrics in electrical performance of oxide thin-film transistors. *J. Mater. Chem. C* **2014**, *2*, 5389.
(29) Tanaka, J.; Ueoka, Y.; Yoshitsugu, K.; Fujii, M.; Ishikawa, Y.; Uraoka, Y.; Takechi, K.; Tanabe, H. Comparison between Effects of PECVD-$SiO_x$ and Thermal ALD-$AlO_x$Passivation Layers on Characteristics of Amorphous InGaZnO TFTs. *ECS J. Solid State Sci. Technol.* **2015**, *4*, Q61−Q65.
(30) Zhu, L.; He, G.; Long, Y.; Yang, B.; Lv, J. Eco-Friendly, Water-Induced $In_2O_3$ Thin Films for High-Performance Thin-Film Transistors and Inverters. *IEEE Trans. Electron Devices* **2018**, *65*, 2870−2876.
(31) Zeumault, A.; Subramanian, V. Mobility Enhancement in Solution-Processed Transparent Conductive Oxide TFTs due to Electron Donation from Traps in High-k Gate Dielectrics. *Adv. Funct. Mater.* **2016**, *26*, 955−963.
(32) Carlos, E.; Branquinho, R.; Kiazadeh, A.; Barquinha, P.; Martins, R.; Fortunato, E. UV-Mediated Photochemical Treatment for Low-Temperature Oxide-Based Thin-Film Transistors. *ACS Appl. Mater. Interfaces* **2016**, *8*, 31100−31108.
(33) Lee, E.; Ko, J.; Lim, K.-H.; Kim, K.; Park, S. Y.; Myoung, J. M.; Kim, Y. S. Gate Capacitance-Dependent Field-Effect Mobility in Solution-Processed Oxide Semiconductor Thin-Film Transistors. *Adv. Funct. Mater.* **2014**, *24*, 4689−4697.
(34) Banger, K.; Warwick, C.; Lang, J.; Broch, K.; Halpert, J. E.; Socratous, J.; Brown, A.; Leedham, T.; Sirringhaus, H. Identification of dipole disorder in low temperature solution processed oxides: its utility and suppression for transparent high performance solution-processed hybrid electronics. *Chem. Sci.* **2016**, *7*, 6337−6346.
(35) Heo, J. S.; Choi, S.; Jo, J. W.; Kang, J.; Park, H. H.; Kim, Y. H.; Park, S. K. Frequency-Stable Ionic-Type Hybrid Gate Dielectrics for High Mobility Solution-Processed Metal-Oxide Thin-Film Transistors. *Materials* **2017**, *10*, 612.
(36) Balakrishna Pillai, P.; Kumar, A.; Song, X.; De Souza, M. M. Diffusion-Controlled Faradaic Charge Storage in High-Performance Solid Electrolyte-Gated Zinc Oxide Thin-Film Transistors. *ACS Appl. Mater. Interfaces* **2018**, *10*, 9782−9791.
(37) Liu, J.; Buchholz, D. B.; Hennek, J. W.; Chang, R. P. H.; Facchetti, A.; Marks, T. J. All-Amorphous-Oxide Transparent, Flexible Thin-Film Transistors. Efficacy of Bilayer Gate Dielectrics. *J. Am. Chem. Soc.* **2010**, *132*, 11934−11942.
(38) Ye, Z.; Yuan, Y.; Xu, H.; Liu, Y.; Luo, J.; Wong, M. Mechanism and Origin of Hysteresis in Oxide Thin-Film Transistor and Its Application on 3-D Nonvolatile Memory. *IEEE Trans. Electron Devices* **2017**, *64*, 438−446.
(39) Heo, J. S.; Jeon, S. P.; Kim, I.; Lee, W.; Kim, Y. H.; Park, S. K. Suppression of Interfacial Disorders in Solution-Processed Metal Oxide Thin-Film Transistors by Mg Doping. *ACS Appl. Mater. Interfaces* **2019**, *11* (51), 48054−48061.
(40) Zhang, H.; Guo, L.; Wan, Q. Nanogranular $Al_2O_3$ proton conducting films for low-voltage oxide-based homojunction thin-film transistors. *J. Mater. Chem. C* **2013**, *1*, 2781.
(41) Zhang, X.; Wang, B.; Huang, W.; Chen, Y.; Wang, G.; Zeng, L.; Zhu, W.; Bedzyk, M. J.; Zhang, W.; Medvedeva, J. E.; Facchetti, A.; Marks, T. J. Synergistic Boron Doping of Semiconductor and Dielectric Layers for High-Performance Metal Oxide Transistors: Interplay of Experiment and Theory. *J. Am. Chem. Soc.* **2018**, *140*, 12501−12510.
(42) Jung, Y.; Yang, W.; Koo, C. Y.; Song, K.; Moon, J. High performance and high stability low temperature aqueous solution-derived Li−Zr co-doped ZnO thin film transistors. *J. Mater. Chem.* **2012**, *22*, 5390.
(43) Smith, J.; Zeng, L.; Khanal, R.; Stallings, K.; Facchetti, A.; Medvedeva, J. E.; Bedzyk, M. J.; Marks, T. J. Cation Size Effects on the Electronic and Structural Properties of Solution-Processed In-X-O Thin Films. *Adv. Electron. Mater.* **2015**, *1*, 1500146.
(44) Aikawa, S.; Mitoma, N.; Kizu, T.; Nabatame, T.; Tsukagoshi, K. Suppression of excess oxygen for environmentally stable amorphous In-Si-O thin-film transistors. *Appl. Phys. Lett.* **2015**, *106*, 192103.
(45) Asahi, R.; Morikawa, T.; Irie, H.; Ohwaki, T. Nitrogen-doped titanium dioxide as visible-light-sensitive photocatalyst: designs, developments, and prospects. *Chem. Rev.* **2014**, *114*, 9824−9852.
(46) Sil, A.; Avazpour, L.; Goldfine, E. A.; Ma, Q.; Huang, W.; Wang, B.; Bedzyk, M. J.; Medvedeva, J. E.; Facchetti, A.; Marks, T. J. Structure−Charge Transport Relationships in Fluoride-Doped Amorphous Semiconducting Indium Oxide: Combined Experimental and Theoretical Analysis. *Chem. Mater.* **2020**, *32*, 805−820.
(47) Cho, S.; Jang, J.-W.; Kong, K.-j.; Kim, E. S.; Lee, K.-H.; Lee, J. S. Anion-Doped Mixed Metal Oxide Nanostructures Derived from Layered Double Hydroxide as Visible Light Photocatalysts. *Adv. Funct. Mater.* **2013**, *23*, 2348−2356.
(48) Zhang, J.; Wu, Y.; Xing, M.; Leghari, S. A. K.; Sajjad, S. Development of modified N doped TiO2 photocatalyst with metals, nonmetals and metal oxides. *Energy Environ. Sci.* **2010**, *3*, 715−726.
(49) Wang, B.; Guo, P.; Zeng, L.; Yu, X.; Sil, A.; Huang, W.; Leonardi, M. J.; Zhang, X.; Wang, G.; Lu, S.; Chen, Z.; Bedzyk, M. J.; Schaller, R. D.; Marks, T. J.; Facchetti, A. Expeditious, scalable solution growth of metal oxide films by combustion blade coating for


https://dx.doi.org/10.1021/jacs.0c05161
J. Am. Chem. Soc. 2020, 142, 12440−12452

flexible electronics. *Proc. Natl. Acad. Sci. U. S. A.* **2019**, *116*, 9230−9238.
(50) Xu, W.; Li, H.; Xu, J. B.; Wang, L. Recent Advances of Solution-Processed Metal Oxide Thin-Film Transistors. *ACS Appl. Mater. Interfaces* **2018**, *10*, 25878−25901.
(51) Lee, W. J.; Park, W. T.; Park, S.; Sung, S.; Noh, Y. Y.; Yoon, M. H. Large-Scale Precise Printing of Ultrathin Sol-Gel Oxide Dielectrics for Directly Patterned Solution-Processed Metal Oxide Transistor Arrays. *Adv. Mater.* **2015**, *27*, 5043−5048.
(52) Ernst, L. F.; Dryer, F. L.; Yetter, R. A.; Parr, T. P.; Hanson-Parr, D. M. Aluminum Droplet Combustion In Fluorine And Mixed Oxygen/Fluorine Containing Environments. *Proc. Combust. Inst.* **2000**, *28*, 871−878.
(53) Park, S.; Kim, C.-H.; Lee, W.-J.; Sung, S.; Yoon, M.-H. Sol-gel metal oxide dielectrics for all-solution-processed electronics. *Mater. Sci. Eng., R* **2017**, *114*, 1−22.
(54) Xu, W.; Wang, H.; Xie, F.; Chen, J.; Cao, H.; Xu, J. B. Facile and environmentally friendly solution-processed aluminum oxide dielectric for low-temperature, high-performance oxide thin-film transistors. *ACS Appl. Mater. Interfaces* **2015**, *7*, 5803−5810.
(55) Limcharoen, A.; Pakpum, C.; Limsuwan, P. An X-ray Photoelectron Spectroscopy Investigation of Redeposition from Fluorine-based Plasma Etch on Magnetic Recording Slider Head Substrate. *Procedia Eng.* **2012**, *32*, 1043−1049.
(56) Zhang, T.; He, Y.; Wang, F.; Li, H.; Duan, C.; Wu, C. Surface analysis of cobalt-enriched crushed products of spent lithium-ion batteries by X-ray photoelectron spectroscopy. *Sep. Purif. Technol.* **2014**, *138*, 21−27.
(57) Saïdi, S.; Guittard, F.; Guimon, C.; Géribaldi, S. Fluorinated acrylic polymers: Surface properties and XPS investigations. *J. Appl. Polym. Sci.* **2006**, *99*, 821−827.
(58) Ferraria, A. M.; Lopes da Silva, J. D.; Botelho do Rego, A. M. XPS studies of directly fluorinated HDPE: problems and solutions. *Polymer* **2003**, *44*, 7241−7249.
(59) Zhang, T.; Park, J. Y.; Huang, W.; Somorjai, G. A. Influence of reaction with $XeF_2$ on surface adhesion of Al and $Al_2O_3$ surfaces. *Appl. Phys. Lett.* **2008**, *93*, 141905.
(60) Mori, T.; Kajihara, K.; Kanamura, K.; Toda, Y.; Hiramatsu, H.; Hosono, H. Indium-based ultraviolet-transparent electroconductive oxyfluoride InOF: ambient-pressure synthesis and unique electronic properties in comparison with $In_2O_3$. *J. Am. Chem. Soc.* **2013**, *135*, 13080−13088.
(61) Peimyoo, N.; Barnes, M. D.; Mehew, J. D.; De Sanctis, A.; Amit, I.; Escolar, J.; Anastasiou, K.; Rooney, A. P.; Haigh, S. J.; Russo, S.; Craciun, M. F.; Withers, F. Laser-writable high-k dielectric for van der Waals nanoelectronics. *Sci. Adv.* **2019**, *5*, eaau0906.
(62) Mibus, M.; Jensen, C.; Hu, X.; Knospe, C.; Reed, M. L.; Zangari, G. Dielectric breakdown and failure of anodic aluminum oxide films for electrowetting systems. *J. Appl. Phys.* **2013**, *114*, No. 014901.
(63) Wang, B.; Zeng, L.; Huang, W.; Melkonyan, F. S.; Sheets, W. C.; Chi, L.; Bedzyk, M. J.; Marks, T. J.; Facchetti, A. Carbohydrate-Assisted Combustion Synthesis To Realize High-Performance Oxide Transistors. *J. Am. Chem. Soc.* **2016**, *138*, 7067−7074.
(64) Chen, Y.; Wang, B.; Huang, W.; Zhang, X.; Wang, G.; Leonardi, M. J.; Huang, Y.; Lu, Z.; Marks, T. J.; Facchetti, A. Nitroacetylacetone as a Cofuel for the Combustion Synthesis of High-Performance Indium-Gallium-Zinc Oxide Transistors. *Chem. Mater.* **2018**, *30*, 3323−3329.
(65) Tressaud, A. Functionalized Inorganic Fluorides: Synthesis, Characterization and Properties of Nanostructured Solids; John Wiley & Sons: 2010.
(66) DuMont, J. W.; George, S. M. Competition between $Al_2O_3$ atomic layer etching and $AlF_3$ atomic layer deposition using sequential exposures of trimethylaluminum and hydrogen fluoride. *J. Chem. Phys.* **2017**, *146*, No. 052819.
(67) Kim, S. E.; Steinbrüchel, C. Metal/fluorinated-dielectric interactions in microelectronic interconnections: Rapid diffusion of fluorine through aluminum. *Appl. Phys. Lett.* **1999**, *75*, 1902.
(68) Donnelly, V. M.; Kornblit, A. Plasma etching: Yesterday, today, and tomorrow. *J. Vac. Sci. Technol., A* **2013**, *31*, No. 050825.
(69) Chupas, P. J.; Corbin, D. R.; Rao, V. N. M.; Hanson, J. C.; Grey, C. P. A Combined Solid-State NMR and Diffraction Study of the Structures and Acidity of Fluorinated Aluminas: Implications for Catalysis. *J. Phys. Chem. B* **2003**, *107*, 8327−8336.
(70) Yagi, T.; Tatemoto, M. A Fluorine-19 NMR Study of the Microstructure of Vinylidene Fluoride-Trifl.uoroethylene Copolymers. *Polym. J.* **1979**, *11*, 429−436.
(71) Tonelli, A. E.; Schilling, F. C.; Cais, R. E. $^{19}F$ NMR Chemical Shifts and the Microstructure of Fluoro Polymers. *Macromolecules* **1982**, *15*, 849−853.
(72) Dec, S. F.; Wind, R. A.; Maciel, G. E. Solid-State Fluorine-19 Nuclear Magnetic Resonance Study of Fluorocarbon Polymers. *Macromolecules* **1987**, *20*, 2754.
(73) Hu, J. Z.; Zhang, X.; Jaegers, N. R.; Wan, C.; Graham, T. R.; Hu, M.; Pearce, C. I.; Felmy, A. R.; Clark, S. B.; Rosso, K. M. Transitions in Al Coordination during Gibbsite Crystallization Using High-Field $^{27}Al$ and $^{23}Na$ MAS NMR Spectroscopy. *J. Phys. Chem. C* **2017**, *121*, 27555−27562.
(74) Cui, J.; Kast, M. G.; Hammann, B. A.; Afriyie, Y.; Woods, K. N.; Plassmeyer, P. N.; Perkins, C. K.; Ma, Z. L.; Keszler, D. A.; Page, C. J.; Boettcher, S. W.; Hayes, S. E. Aluminum Oxide Thin Films from Aqueous Solutions: Insights from Solid-State NMR and Dielectric Response. *Chem. Mater.* **2018**, *30*, 7456−7463.
(75) MacKenzie, K. J. D.; Smith, M. E. Multinuclear Solid-State Nuclear Magnetic Resonance of Inorganic Materials; Elsevier: 2002.
(76) Heinemann, M. D.; Berry, J.; Teeter, G.; Unold, T.; Ginley, D. Oxygen deficiency and Sn doping of amorphous $Ga_2O_3$. *Appl. Phys. Lett.* **2016**, *108*, No. 022107.
(77) Dou, X.; Li, Y.; Mohan, D.; Pittman, C. U.; Hu, M. A property-performance correlation and mass transfer study of As(v) adsorption on three mesoporous aluminas. *RSC Adv.* **2016**, *6*, 80630−80639.
(78) Isobe, T.; Watanabe, T.; d'Espinose de la Caillerie, J. B.; Legrand, A. P.; Massiot, D. Solid-state $^1H$ and $^{27}Al$ NMR studies of amorphous aluminum hydroxides. *J. Colloid Interface Sci.* **2003**, *261*, 320−324.
(79) Paluch, P.; Potrzebowska, N.; Ruppert, A. M.; Potrzebowski, M. J. Application of (1)H and (27)Al magic angle spinning solid state NMR at 60kHz for studies of Au and Au-Ni catalysts supported on boehmite/alumina. *Solid State Nucl. Magn. Reson.* **2017**, *84*, 111−117.
(80) Khabibulin, D. F.; Papulovskiy, E.; Andreev, A. S.; Shubin, A. A.; Volodin, A. M.; Zenkovets, G. A.; Yatsenko, D. A.; Tsybulya, S. V.; Lapina, O. B. Surface Hydroxyl OH Defects of $\eta$-$Al_2O_3$ and $\chi$-$Al_2O_3$ by Solid State NMR, XRD, and DFT Calculations. *Z. Phys. Chem.* **2017**, *231*, 809−825.
(81) Tsao, J. Y.; Chowdhury, S.; Hollis, M. A.; Jena, D.; Johnson, N. M.; Jones, K. A.; Kaplar, R. J.; Rajan, S.; Van de Walle, C. G.; Bellotti, E.; Chua, C. L.; Collazo, R.; Coltrin, M. E.; Cooper, J. A.; Evans, K. R.; Graham, S.; Grotjohn, T. A.; Heller, E. R.; Higashiwaki, M.; Islam, M. S.; Juodawlkis, P. W.; Khan, M. A.; Koehler, A. D.; Leach, J. H.; Mishra, U. K.; Nemanich, R. J.; Pilawa-Podgurski, R. C. N.; Shealy, J. B.; Sitar, Z.; Tadjer, M. J.; Witulski, A. F.; Wraback, M.; Simmons, J. A. Ultrawide-Bandgap Semiconductors: Research Opportunities and Challenges. *Adv. Electron. Mater.* **2018**, *4*, 1600501.
(82) Lu, H.; Meng, X. Correlation between band gap, dielectric constant, Young's modulus and melting temperature of GaN nanocrystals and their size and shape dependences. *Sci. Rep.* **2015**, *5*, 16939.
(83) Czaja, W.; Gränacher, I. A relation between the gap energy and the dielectric constant in semiconductors of diamond structure. *Helv. Phys. Acta.* **1963**, *36*, 8.
(84) Sharma, A. C. Size-dependent energy band gap and dielectric constant within the generalized Penn model applied to a semiconductor nanocrystallite. *J. Appl. Phys.* **2006**, *100*, No. 084301.
(85) Klauk, H.; Halik, M.; Zschieschang, U.; Schmid, G.; Radlik, W.; Weber, W. High-mobility polymer gate dielectric pentacene thin film transistors. *J. Appl. Phys.* **2002**, *92*, 5259−5263.


https://dx.doi.org/10.1021/jacs.0c05161
J. Am. Chem. Soc. 2020, 142, 12440−12452

(86) Ruzgar, S.; Caglar, M. Use of bilayer gate insulator to increase the electrical performance of pentacene based transistor. *Synth. Met.* **2017**, *232*, 46−51.
(87) Rahmanudin, A.; Tate, D. J.; Marcial-Hernandez, R.; Bull, N.; Garlapati, S. K.; Zamhuri, A.; Khan, R. U.; Faraji, S.; Gollu, S. R.; Persaud, K. C.; Turner, M. L. Robust High-Capacitance Polymer Gate Dielectrics for Stable Low-Voltage Organic Field-Effect Transistor Sensors. *Adv. Electron. Mater.* **2020**, *6*, 1901127.
(88) Young, N. D.; Gill, N. D. Y. a. A. Water-related instability in TFTs formed using deposited gate oxides. *Semicond. Sci. Technol.* **1992**, *7*, 1103−1108.
(89) Chang, Y.-H.; Yu, M.-J.; Lin, R.-P.; Hsu, C.-P.; Hou, T.-H. Abnormal positive bias stress instability of In−Ga−Zn−O thin-film transistors with low-temperature $Al_2O_3$ gate dielectric. *Appl. Phys. Lett.* **2016**, *108*, No. 033502.


https://dx.doi.org/10.1021/jacs.0c05161
J. Am. Chem. Soc. 2020, 142, 12440−12452